Hopping Charge Transport in Honeycomb Carbon Network Structures

L. V. Govor and J. Parisi

Faculty of Physics, Department of Energy and Semiconductor Research, University of Oldenburg, D-26111 Oldenburg

Reprint requests to Prof. J. P.; Fax: ++49-441-798.3326, E-mail: parisi@ehf.uni-oldenburg.de

Honeycomb-type nitrocellulose network patterns based on a hexagonal elementary cell with a diameter of about 2 μm have been fabricated by means of a self-organized preparation process. Our method takes advantage of the spreading of a drop of the initial polymer solution on the surface of distilled water cooled down to a temperature of 3 to 5 °C and the subsequent influence of the water vapor (i.e., air with relative humidity in the range from 19 to 100 %) on the resulting polymer thin film. In the following, an advanced structuring model is proposed capable to explain the morphology and growth of the individual cells inside the network obtained in the experiment. The values of their electrical conductivity extending steadily from insulator to metal behavior distinctly change via heat treatment under vacuum conditions and at process temperatures ranging from 600 to 1000 °C. Upon variation of the ambient temperature T from 4.2 to 295 K, four different transport mechanisms can be unveiled. For the case of carbon nets, the conductivity of which is far beyond the metal-insulator transition, the specific resistivity ρ depends on T as $\rho(T) \propto T^{-b} \exp\left(\left[T_0/T\right]^{1/p}\right)$. In the low-temperature regime, a Coulomb gap in the density of states located near the Fermi energy level occurs, that means, the characteristic value of the exponent is $p = 2$. At high temperatures, the pre-exponential part $\rho(T) \propto T^{-b}$ dominates. In the intermediate temperature range, we disclose Mott's hopping law with $p = 3$. The electrical field dependence of the variable range hopping process of porous carbon networks is examined in the region of validity of the law $\ln \rho(T) \propto T^{-1/2}$. We show that the electrical conductivity σ caused by thermally nonactivated charge carriers at high fields complies with $\ln \sigma(E) \propto E^{-1/3}$. The current density j changes as $\ln j(E) \propto E^{-1/6}$. The temperature dependence of the threshold electrical field E_{th}, which characterizes the transition from the low-field to the high-field regime, follows $E_{\mathrm{th}} \propto T^{1.5}$.

Key words: Self-organized Network Structures; Variable Range Hopping Charge Transport; Metal-insulator Transition, Coulomb Gap.

1. Introduction

It is well known that the low-temperature behavior of the specific resistivity $\rho(T)$ of amorphous semiconductors, granular thin films, porous materials, and other disordered media can usually be described by the elementary process of variable range hopping (VRH) of charge carriers. The degree of doping in those disordered systems is selected in such a way that the value of the electrical conductivity lies in the vicinity of the metal-insulator transition (MIT) on the insulating side. Such a dependence follows the equation

$$\rho(T) = \rho_0 \exp\left[\left(T_0/T\right)^{1/p}\right], \qquad (1)$$

where ρ_0 and T_0 denote material parameters which do not (strongly) depend on temperature; T_0 is determined by the density of localized states, $N(E)$, near the Fermi energy E_{F}. The characteristic value p depends on both the dimensionality and the degree of disorder that governs the medium investigated [1]. The values $p = 4$, $p = 3$, and $p = 2$ correspond to VRH in three-, two-, and one-dimensional (3D, 2D, and 1D) disordered systems, respectively [2]. The characteristic value $p = 2$ can be observed also for 3D and 2D cases and is then explained with the model of Efros and Shklovskii [3 - 5]. The latter considers long-range Coulomb interactions between electrons that come along from different centers of localization near the Fermi level. As a result, a Coulomb gap

in the density of states, $N(E)$, near the Fermi energy develops. For 3D, the gap obeys the dependence $N(E) \propto (E - E_F)^2$. At the Fermi energy E_F, we have $N(E) = 0$.

Theoretical investigations of the current-voltage characteristics of amorphous semiconductors, the ohmic conductivity of which in the low-temperature regime is described by (1), have been carried out in earlier work [6 - 10]. According to the calculations of Hill [6] as well as Pollak and Riess [7], the relation

$$\sigma(E) = \sigma(0) \exp\left[\frac{CeEr_m}{k_BT}\right] \quad (2)$$

should be fulfilled by the conductivity $\sigma(E) = j(E)/E$ in case of the boundary condition $eEr_m > k_BT$. Here, j is the current density, E the electrical field, e the electron charge, $l = Cr_m$ the hopping length, $r_m = a\xi_c/2$ the maximum hopping length on the percolation paths, a the localization radius of the wave function, $\xi_c = (T_0/T)^{1/p}$ the percolation threshold (at $\xi_c \gg 1$), k_B Boltzmann's constant, and C a constant, the value of which was determined to 0.8 (given in [6]) and 0.17 (given in [7]). On the other hand, the work of Apsley and Hughes [8] receives the dependence $\ln \sigma(E) \propto E^2$ for the same electrical field range. At high electrical fields, the activationless hopping conductivity has been predicted by Mott [9]. Accordingly, the current density versus electrical field characteristic was found to be [11]

$$j(E) \propto \exp\left[-\left(\frac{E_0}{E}\right)^{1/m}\right]. \quad (3)$$

Note that the value of m – according to [11] – corresponds with the value of p from (1) just at $p = 4$. The equality $m = p = 4$, therefore, provides evidence that, in the model examined, the high electrical field plays the same role as the temperature does within the regime of ohmic conductivity. Experimental work [12, 13] has confirmed the above conclusion, both for the case $m = p = 4$ (3D) and the case $m = p = 3$ (2D). Rentzsch et al. [14] observed experimentally the equality $m \approx p \approx 1.3 - 1.6$ for poly-crystalline ZnSe films having a thickness of 1 μm. VRH in a parabolic quasi-gap at high electrical fields was investigated in [15 - 17], where the equality $m = p = 2$ has been determined. On the other hand, the same measurements performed on $Ge_{1-x}Cu_x$ amorphous thin films [18] led to the values $p = 2$ and $m = 4$.

The prevailing ambiguity of the above statements concerning the character of the current-voltage (resp. current density versus electrical field) characteristics of amorphous semiconductors, as described by (1), marked the starting point of the present work. Moreover, for our analysis of the charge transport process, we have chosen micrometer-size porous carbon membranes with highly ordered honeycomb structures. The electrical conductivity of the membranes in the range from insulator to metal behavior could be changed via heat treatment under vacuum conditions and at different process temperatures.

For producing such membranes, there exists a huge variety of preparation methods [19]. Self-organization (or, as it is often called, self-assembly) may offer some advantages in this field: the patterning process can function in different media, and cost-intensive large-scale technology is not necessary. By the help of self-organized processes, one is able to develop distinct structures with a regular geometrical form (e. g., networks with hexagonal elementary cells). Nowadays, the ordered mesoporous solids with nanoscale pore sizes are fabricated by self-organization of spherical micelles from a diblock copolymer system in a selective solvent [20]. The class of mesoporous materials can be formed by colloidal templating [21, 22]. Colloidal crystals of polystyrene or silica spheres are embedded in a fluid that fills the space between the spheres. Next, the templating spheres are removed, and one awaits the creation of a porous solid where the dimension of the pores matches those of the templating spheres.

Water-assisted formation of ordered mesoporous membranes has been described in the papers [23 - 28]. In that case, the membranes are formed by condensation of water vapor on the fluid polymer solution film and by subsequent evaporation of a solvent from the polymer solution. Recently, we have developed a preparation method that allows for membrane formation with evenly shaped hexagonal cells having a diameter of about 1 - 2 μm [29 - 31]. There, the technology how to get mesoporous membranes from different polymers has been reviewed in detail. Simultaneously, some effort was undertaken to interpret the self-organizing mechanism of patterning by thermodynamic processes that take place between water droplets on the surface of the fluid polymer solution. We have suggested that the stabilization of water droplets on a fluid surface is indispensable for ordered structure formation. In the following, the most

important stabilization parameters are discussed that can influence the growth of condensing water droplets on the fluid polymer solution layer and their interaction between each other.

2. Experimental Formation of Polymer Honeycomb Structures

2.1. Spreading of one Liquid on Another

For producing a self-organized honeycomb polymer network, we have developed a four-step method. Figure 1 illustrates these steps: (a) deposition of one drop of polymer solution (liquid F1) on the cooled water surface (liquid F2, 3 - 5 °C); (b) spreading of one drop of polymer solution to an extremely thin layer; (c) interaction of water vapor (air with 100, 75, 32, or 19 % relative humidity at 20 °C) with the polymer thin film surface for self-structuring the spatial distribution of the lateral water droplets and subsequently generating the polymer network; (d) mechanical removal of the structured network from the liquid and potential fixation on a substrate by annealing.

The condition for the spreading of a drop of liquid F1 on the surface of liquid F2 derives from thermodynamic arguments [32]

$$\gamma_{F2/G} > \gamma_{F1/G} + \gamma_{F1/F2}, \tag{4}$$

where $\gamma_{F1/F2}$, $\gamma_{F1/G}$, and $\gamma_{F2/G}$ denote the surface tension between the liquids F1 and F2, between liquid F1 and gas G (in our case, G is air), and between liquid F2 and gas G, respectively. The degree of spreading of a film of liquid F1 over liquid F2 characterizes the spreading coefficient which reads [32]

$$S_{F1/F2} = \gamma_{F2/G} - \gamma_{F1/G} - \gamma_{F1/F2}. \tag{5}$$

For $S_{F1/F2} > 0$, total spreading is achieved, i.e., the liquid drop F1 will cover the whole surface of the liquid F2 and, thereby, form a monomolecular layer at the edge. For $S_{F1/F2} < 0$, there is no spreading.

2.2. Production of Nitrocellulose Networks

The coating of one drop of 1% nitrocellulose solution in amyl acetate on the cooled water surface leads to a complete spreading along that surface [30]. The surface tension coefficient of the 1% nitrocellulose solution in amyl acetate amounts to $\gamma_{F1/G}(20\ °C) =$
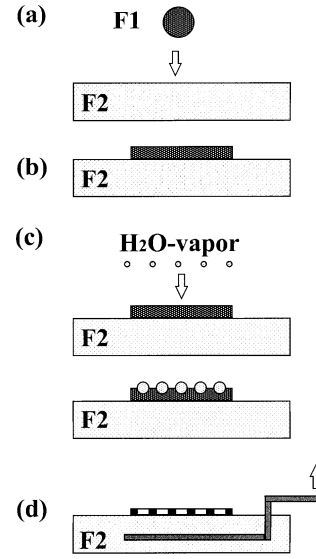

Fig. 1. Formation of a self-organized honeycomb polymer structure: (a) deposition of one drop of polymer solution F1 on the cooled water surface F2; (b) spreading of one drop of polymer solution to a thin layer; (c) water vapor condensing on the polymer film surface; growing of water droplets and building of the compact hexagonal structure, i.e., polymer network; (d) drying of the polymer network and transfer from the water surface to a fixed substrate.

24.6 mN/m. Distilled water cooled down to 3 - 5 °C possesses a surface tension coefficient of $\gamma_{F2/G} = 74.9$ mN/m. For the surface tension of the 1% nitrocellulose solution in amyl acetate on water, we take the value $\gamma_{F1/F2} = 12$ mN/m. The demand for total spreading of one drop of the 1% nitrocellulose solution in amyl acetate on the cooled water surface is fulfilled, because we have $S_{F1/F2} = 38.3$ mN/m.

The size of the spread thin polymer layer in the vessel (with a diameter of 93 mm) was 70 mm. Since the volume of the spread drop came to 15 μl, the thickness of the resulting spread liquid polymer layer can be estimated to be 3.9 μm. Our thin film was subject to the influence of water vapor which indicates the self-organized formation of a honeycomb network structure. The size of the water droplets has not been kept under control. However, the relative humidity of air was taken constant to about 75% at a temperature of 20 °C. Depending on the time elapsed after the water vapor has started to affect the polymer film, one obtains a variety of network structures distinguished both in form and size. During our experiments, the above time span changed between 1 and 60 s. In a final step, after having dried the network,

it was transferred from the water surface to a sapphire substrate.

2.3. Structural Forms of Self-assembled Nitrocellulose Networks

In the following, let us look at the network structures fabricated by the above procedure. After depositing the water vapor on the polymer layer and drying the latter, a fractal-like geometry appears, i.e., areas (in the form of strips) with network structures and areas without them come to light. The majority of the structured strips was distributed at the edge of the polymer layer and normally had a width of 0.5 mm and a length of 20 mm. The network strips can be connected with or separated from each other. Figure 2(a) gives a scanning electron microscope (SEM) picture of hexagonal nitrocellulose cells resulting from a fragment. In this case, the water vapor was coated 10 s after having spread the polymer layer onto the cooled water surface. Note the strong spatial homogeneity and reproducibility of the individual cells inside the network structure. For a more detailed look at the geometry, a blow-up picture embracing only few elementary cells, is displayed in Figure 2(b). The diameter of the cell (i.e., the distance between the interknot connection centers) amounts to 2.6 μm, and the width of the interknot connection to about 0.4 μm. The cross-section of the interknot connection perpendicular to the photograph plane offers the view of a T-like shape. The latter means that each hexagonal cell lies on a hexagonal base, also having extremely thin side walls. The height of the base is 0.5 μm. Each one of these six side walls represents some kind of a frame with various thickness along the circuit on which a thin polymer film is stretched. In most cases, the polymer film unveils an oval aperture in the middle of the frame.

Few structured large strips have a different diameter of the single cell on their edges (for example, 2 μm) and in their center (for example, 6 μm). Figure 3 demonstrates SEM images of different fragments of one structured strip after annealing for one hour at a temperature of 950 °C under vacuum conditions. Figure 3(a) shows a network fragment between the edge and the center of the strip, where the cell diameter varies from 2 to 4 μm. Obviously, the cross-section of the interknot connection perpendicular to the photograph plane does not represent the T-like shape mentioned above, i. e., the interknot connection merges

after annealing. As a result, we observe an almost two-dimensional cell configuration. Figure 3(b) illustrates a network fragment in the center of the strip after annealing. Here, we have three-dimensional elementary cells of a carbon network pattern obtained from a corresponding nitrocellulose structure after annealing. In case where the latter cells have a relatively large diameter, the total network extends over an area of about $30 \times 30 \ \mu m^2$. Apparently, the upper and lower hexagonal cells (one placed on the top of the other) — both with a diameter of 6 μm — are practically equal. The relating two cells are connected only at the corners (cf. Fig. 3(b)). The height of the junction between the upper and the lower cells is approximately 1.5 μm. The diameter of the interknot connection amounts to about 0.25 μm.

Figure 4(a) gives another SEM image of a nitrocellulose network with a different kind of structural form (compared to the one of Fig. 3) that we have obtained when coating the water vapor 60 s after spreading the polymer layer onto the cooled water surface. Take note of the parallel orientation (in all three directions) of the interknot connections. For a better determination of the geometrical parameters, a blow-up of Fig. 4(a), confined to only few elementary cells, is displayed in Figure 4(b). It turns out that the cross-section of the interknot connection is somewhat plate-shaped. The width of the interknot connection amounts to approximately 1.5 μm, and the height of the "plate walls" to about 0.25 μm. Inside the cell, one can perceive the breakthrough of the thin polymer film. We point out that the cross-section of the interknot connection of the latter structure does not have a T-like shape (in contrast to the one in Fig. 2).

3. Model for the Formation of Honeycomb Structures in Polymer Films

3.1. Spreading Coefficient for two Mutually Saturated Liquids

When the fluid substance is placed at a liquid-air interface, it may spread out to a thin film. That happens when we deposit a liquid with low surface tension on a liquid with high surface tension. One has a positive spreading coefficient for all of our polymer solutions in amyl acetate. In Sect. 2, where we have determined the spreading coefficient $S_{F1/F2}$, (5), we took the surface tension values of the amyl acetate solution and water for the pure liquids. However, if two liquids
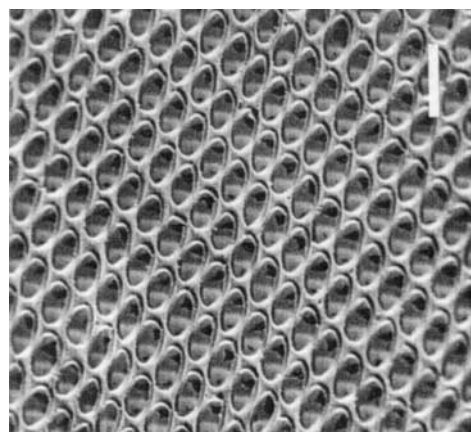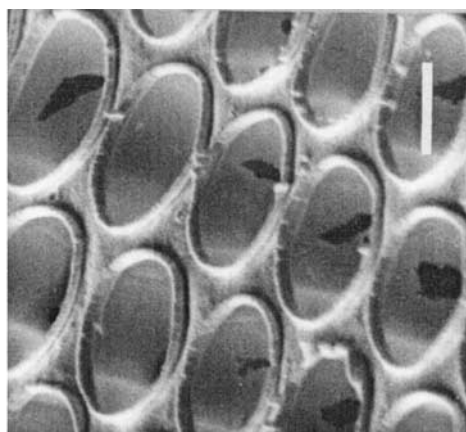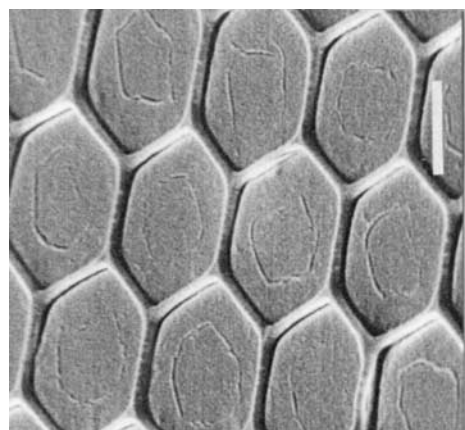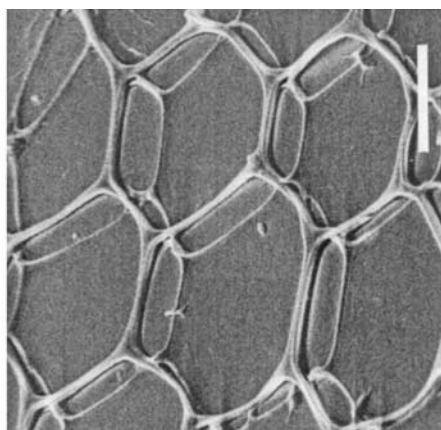
Fig. 4. SEM images of a nitrocellulose network with plate-shaped interknot connections which were prepared via coating the water vapor 60 s after having spread the polymer layer onto the cooled water surface. Scale bars: (a) 5 μm; (b) 2μm.

Fig. 3. SEM images of different areas of one carbon network with (a) a two-dimensional elementary cell and (b) a three-dimensional elementary cell which was heated for one hour at a temperature of 950 °C under vacuum conditions. The network was prepared via coating the water vapor 10 s after having spread the polymer layer onto the cooled water surface. Scale bars: (a) 2 μm; (b) 4μm.
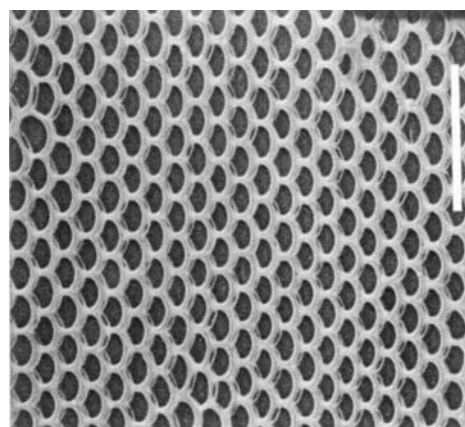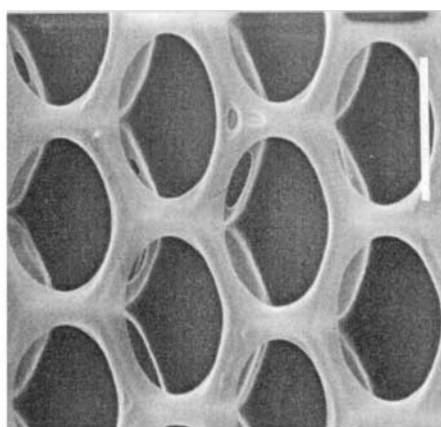
Fig. 2. SEM images of a nitrocellulose network which was prepared via coating the water vapor 10 s after having spread the polymer layer onto the cooled water surface. Scale bars: (a) 10μm; (b) 2μm.

are in contact, they will become mutually saturated, so that $\gamma_{F2/G}$ will change to $\gamma_{F2(F1)/G}$, and $\gamma_{F1/G}$ to $\gamma_{F1(F2)/G}$. The symbol F1 (F2) means that liquid F1 is saturated with liquid F2. The corresponding spreading coefficient has the symbol $S_{F1(F2)/F2(F1)}$ and can be determined as [32]

$$S_{F1(F2)/F2(F1)} = \gamma_{F2(F1)/G} - \gamma_{F1(F2)/G} - \gamma_{F1/F2}. \quad (6)$$

In this case, for the solution of nitrocellulose in amyl acetate on the water surface (at 20 °C), we have $S_{F1(F2)/F2(F1)} = 39.5$ mN/m $- 26.9$ mN/m $- 12$ mN/m $= 0.6$ mN/m, i.e., the final spreading coefficient is positive. The values of the surface tension coefficients were determined using a stalagmometer. This instrument consists of a capillary tube through which the polymer solution flows, which enables the counting of the number of droplets and, therefore, the derivation of the surface tension.

3.2. Water Droplet on the Fluid Polymer Layer

3.2.1. Water Droplet before the Contact with the Polymer Layer

Next, we look in a more detailed way at the lay on of the steam, representing one crucial factor for the patterning process. Since the cell diameter of our networks is about 2 μm, we investigate the shape of a water droplet with the same diameter, before it dissolves on the surface of the polymer thin film. We have to compare two pressure quantities: the first one is the capillary pressure P_L which gives rise to the spherical shape of the droplet, the second one, the so-called gravitation pressure P_G, causes the flattening of the droplet. The capillary pressure can be calculated by the well-known formula $P_L = 2\gamma_{F2/G}/R_d$, with R_d giving the droplet radius. In our case we obtain $P_L = 1.4 \cdot 10^9$ Pa. If the contact plane between the droplet and the polymer thin film is approximately πR_d^2, we can determine $P_G = m_d g/\pi R_d^2$ with the water droplet mass $m_d = 4\pi R_d^3 \rho_d/3$ (ρ_d is the water density). Finally, one ends up with $P_G = 1.3 \cdot 10^{-2}$ Pa. If we compare both types of pressure, it turns out $P_L \gg P_G$. That means that the water droplet has a spherical shape before laying on the surface of the polymer solution.

3.2.2. Water Droplet after the Contact with the Polymer Layer

The first moment the water droplet contacts the polymer layer is sketched in Fig. 5(a): If the droplet
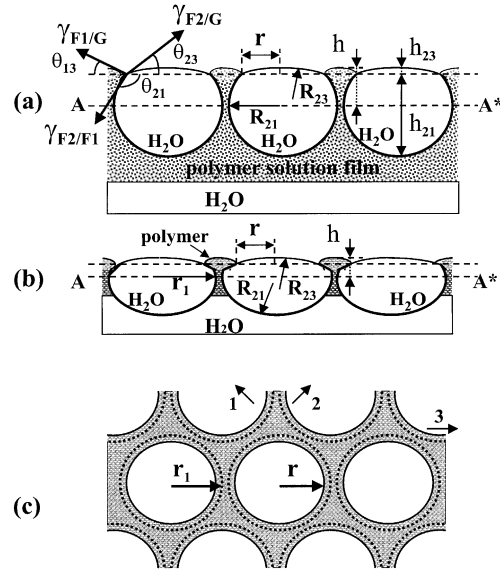

Fig. 5. Model for the lay on of the water steam on the polymer layer: (a) process of envelopment of the water droplet by the polymer layer; the thin film on the surface of the water drop indicates a monomolecular polymer layer; (b) moment of the first contact of the water drop with the cooled water surface; (c) model structure of the network according to (b) in the plane of the polymer layer.

comes into touch with the surface, the destruction of the droplet will start. The angles θ_{21} and θ_{23}, in this case, are nonequalized boundary angles, because they experience variations in the development of further physical and chemical processes that take place at the phase boundary.

Water is a denser medium than amyl acetate (0.87 g/cm^3), but the water droplets do not sink as a consequence of a subtle balance between buoyancy, droplet weight, and capillary forces [33]. The droplets are situated at the interface between the fluid polymer layer and air. Only a small part of the droplet is located above the surface of the fluid polymer layer. The water droplets on the fluid polymer layer do not coalesce immediately after they touch, because they are separated by a thin film of the polymer solution. We assume that a thin polymer film (only a few monomolecular layers thick) develops on the top of the droplets, similar to the spreading of the polymer solution drop on the water surface. The latter thin film on top of the water droplet might be a reason for the growth retarding of the water droplets and, therefore, a key parameter for the regulation of the droplet size. In addition, we suggest that water droplets in the polymer solution

are covered with a solid polymer layer at the interface between the two liquids. Experimentally these layers, which are characterized by bursting holes (black), can be seen in Fig. 4; the water flows out of them after the solvent has evaporated. Such a layer prevented coalescence of water droplets, i.e., the precipitation of nitrocellulose at the interface between the polymer solution and the water droplets provides the basis for the formation of a compact hexagonal structure of water droplets. In our model scheme of Fig. 5(a), the precipitation layer is illustrated as a solid line between the water droplets and the polymer solution. Similar results have been obtained for another experimental situation, where water droplets are deposited on the surface of a solution of poly(p-phenylene) block polysterene in carbon disulfide [26].

In Fig. 5(a), the corresponding forces are indicated, which come into play at the above phase boundary. These forces, converted to the length unit of the wetting line, are equivalent to the corresponding quantities of the surface tension. From the condition that gives the balance of the surface tensions, the equilibrium state at the edge circumference of the contact between the water droplet and the polymer layer can be described by the two equations

$$\gamma_{F1/G} \cos \theta_{13} = \gamma_{F2/G} \cos \theta_{23} + \gamma_{F2/F1} \cos \theta_{21}, \quad (7)$$

$$\gamma_{F2/G} \sin \theta_{23} + \gamma_{F1/G} \sin \theta_{13} = \gamma_{F2/F1} \sin \theta_{21}, \quad (8)$$

where the angles θ_{ij} are defined in Figure 5(a). Equation (7) treats the balance of forces in the plane of the polymer layer, and (8) the balance of forces directed perpendicular to it.

For the subsequent qualitative discussion of the shape of the water droplet (the angles θ_{ij} are defined in Fig. 5(a)), only the initial values of the surface tension γ are used. The water droplet shape on the surface of paraffin oil has been studied by Knobler and Beysens [34], and on the surface of carbon disulfide by Pitois and Francois [26]. They have suggested that the water droplet has the form of a strongly asymmetric lens, the major part of which is nearly a complete sphere suspended from the surface. Based on these studies and our experimental results displayed in Figs. 2 and 4, the shape of the water droplet located on the surface of the polymer solution in amyl acetate has been accordingly sketched in Figure 5(a). In our case, the capillary pressure in the water droplet is drastically higher than the gravitation pressure ($P_L \gg P_G$), i.e.,

the influence of gravity forces on the droplet shape can be neglected. That means that the small water droplet on the fluid polymer layer is composed of two spherical segments (see Fig. 5(a)), the angles θ_{ij} and radii R_{ij} of which can be determined by the surface tension forces [35]

$$\cos \theta_{ij} = [1 + (\gamma_{ij}/\gamma_{jk})^2 - (\gamma_{ik}/\gamma_{jk})^2]/2(\gamma_{ij}/\gamma_{jk}), (9)$$

$$R_{ij}/r = 1/\sin \theta_{ij}, \quad (10)$$

$$h_{ij}/r = (1 - \cos \theta_{ij})/\sin \theta_{ij}, \quad (11)$$

where θ_{ij}, R_{ij}, h_{ij}, and r are defined as illustrated in Figure 5(a). It should be noted that, in the case of an extremely small lens, Princen [35] has assumed that the angle θ_{13} is zero. In our case of a relatively thin polymer fluid layer, the exact determination of the angles θ_{ij} from (9) is not that easy, because the initial values of the parameters $\gamma_{F2/G}$, $\gamma_{F1/G}$, and $\gamma_{F2/F1}$ alter with time. On the other hand, for the case of a water droplet placed on the surface of paraffin oil, the angles θ_{ij} were measured by Knobler and Beysens [34]. They observed values in the range $\theta_{21} = 135° - 140°$ and $\theta_{23} = 20° - 25°$. The fluid properties (i.e., surface tension, density) of amyl acetate and paraffin oil are comparable. The force $\gamma_{F1/G} \sin \theta_{13} \times 2\pi r$ in (8) does not permit the water droplet to sink into the polymer solution layer, i.e., the angle θ_{13} cannot be zero. On the other hand, for a water droplet with a diameter of $2 \ \mu$m as in our case, the deviation from a horizontal line is necessarily not particularly strong, in order to provide the upward force.

At the moment of the first contact between the water droplet and the fluid polymer layer, the force $\gamma_{F2/G} \sin \theta_{23}$ for achieving the equilibrium state (described by (8)) tends to pull the polymer layer onto the water droplet. The water droplet then more and more penetrates the polymer layer. The envelopment of the water droplet by the polymer layer will take place as long as the angles θ_{21}, θ_{23}, and θ_{13} (or the radii of the surface curvatures, R_{21} and R_{23}, see Fig. 5(a)) experience variations such that the pressure inside the water droplet caused by the surface curvature of the boundary between water and air is equal to the pressure which results from the surface curvature at the boundary between water and polymer layer. Their balance can be expressed mathematically by

$$\gamma_{F2/G}/R_{23} = \gamma_{F2/F1}/R_{21}, \quad (12)$$

where R_{23} and R_{21} are the radii of the water droplet at the boundary between water and air and between water and the polymer layer, respectively. If we substitute the above values $\gamma_{F2/G} = 71$ mN/m and $\gamma_{F2/F1} = 12$ mN/m in (12), we obtain $R_{23}/R_{21} \approx 6$ for nitrocellulose solutions in amyl acetate. That means that pressure equality in the lower and upper part of the water droplet at thermodynamical equilibrium can only be guaranteed if the radius R_{23} exceeds R_{21} by a factor of six (see Fig. 5(a)).

3.2.3. Formation of Breath Figures

The formation of the observed hexagonally arranged layer of the water droplets on the liquid polymer layer can be explained as follows. With the condensation of the water vapor on the cold surface of the liquid, the water droplets form to a pattern of breath figures [36 - 39], the geometry of which can be very different. The basic physical arguments supporting the development of breath figures on the fluid surfaces were discussed by Knobler et al. [34] and Steyer et al. [23, 40]. They suggest that breath figures on fluid surfaces evolve through three stages: (a) initial stage, when the water droplets are isolated such that they do not strongly interact, and the average droplet radius $\langle R_d \rangle$ grows with time t_d as $\langle R_d \rangle \propto t_d^{1/3}$; (b) cross-over stage, when the surface coverage is high and the rate of the droplet growth increases; (c) coalescence dominated stage, when the surface coverage is high and constant, and the droplet radius grows as $\langle R_d \rangle \propto t_d$.

The attractive force F between two water droplets on the surface of the polymer solution separated by a distance l_d was determined by Steyer et al. [23] and Chan et al. [33]:

$$F = (4\pi R_d^6 \rho_a^2 g^2 / 3 l_d \gamma_{F1/G}) \tag{13}$$

$$\cdot [1/\rho_s + 0.25(1 - k^2)^{1.5} - 0.75(1 - k^2)^{0.5}]^2,$$

where R_d denotes the radius of the droplets, ρ_a the absolute density of the polymer solution, g the earth's gravitational acceleration, $\gamma_{F1/G}$ the surface tension between the polymer solution and air, ρ_s the relative density of the polymer solution compared to air, $k = r/R_{21}$, where r and R_{21} are radii as illustrated in Figure 5(a). Equation (13) holds if the bond number $B_0 = R_d^2 \rho_a g / \gamma_{F1/G}$ is small enough (i.e., < 0.1, see [33]). In our case, B_0 is of the order of 10^{-6} for all polymer solutions and water droplets with a diameter of 2 μm. Parameter k characterizes the contact angles of the water droplet with the surface of the polymer solution and is highly sensitive to the wetting properties between water and the polymer solution. Steyer et al. [23] have proposed that the formation of a hexagonal structure for the water droplets occurs when the parameter k ranges between 0.4 and 0.8. The hexagonal structure disappears when k varies from 0.2 to 0.4.

In our case, an exact determination of k and the corresponding force F is not that easy, because initial values of the parameters $\gamma_{F2/G}$, $\gamma_{F1/G}$, $\gamma_{F2/F1}$, and ρ_a alter with time. We are interested to consider only some tendency according to (13) with initial values of the surface tension γ. Equation (13) tells us that, upon altering k, the force can increase considerably, i.e., k can play the role of a key parameter for the formation of a hexagonal structure of water droplets. For the present case, the value of k can be estimated from (10). Taking the angle $\theta_{21} = 135°$, one calculates $k \approx 0.7$. The corresponding experimental value of k, which derives from the geometrical size of a single cell in Fig. 2, is equal to 0.8 for a nitrocellulose network. From (11) we determine for $\theta_{23} = 20°$ and $r \approx 0.7$ μm (i.e., $R_{21} = 1$ μm) the parameter $h_{23} \approx 0.1$ μm, and for $\theta_{21} = 135°$ the parameter $h_{21} \approx 1.7$ μm.

With increasing $\gamma_{F1/G}$, the attractive force F between the two water droplets decreases, and the corresponding distance l_d between the droplets increases. Our finding can be corroborated in Figs. 2 and 4. The interknot connections of the nitrocellulose network, obtained when the water vapor was coated 10 s after spreading the polymer film, amounts to 0.25 μm (see Fig. 2). Turning to Fig. 4, where the time period between spreading and subsequent coating has been extended to 60 s, the relating width of the interknot connections increases to about 1.0 μm, i.e., the surface tension of the nitrocellulose solution increases with the evaporation time of the solvent.

During the drying process of the polymer film, the water droplets approach the cooled water surface. In Fig. 5(b), the contact between the water droplet and the cooled water surface together with the corresponding variation of the radii R_{23} and R_{21} are displayed schematically. Between the water droplet and the cooled water surface we find a thin precipitation polymer film. The radius R_{21} will be enlarged, since the lower part of the water droplet which is in contact with the cooled water surface (more precisely, with the thin polymer film) will have a flat boundary plane. Figure 5(b) features the cross-section of the interknot

connection of one cell of the polymer network which develops between two neighboring water droplets. Comparison of Figs. 2 and 5(b) yields a pronounced similarity between the cross-section of the experimentally prepared elementary cell of the polymer network and the one of the modelled cell. From these pictures we conclude that the minimum thickness of the polymer layer in the middle of the frame (i.e., the base plate) corresponds to the minimum distance between the water droplets near the AA* line. For the case of nitrocellulose in amyl acetate, the above distance is probably a few monomolecular layers thick.

3.2.4. Formation of 2D and 3D Networks

The appearance of small areas ($30 \times 30\,\mu m^2$) in the central region of the nitrocellulose network strips (see Fig. 2) with elementary cells of the form displayed in Fig. 3(b) derives from some size gradient of the water vapor droplets. The formation of a hexagonally arranged pattern of water droplets on the liquid polymer layer with the above size gradient can be explained as follows. Due to the water vapor condensation on the cold surface of the liquid in the first moment, the water droplets conform to the islands which later on build the breath figures [36 - 39]. The islands attract each other in a much stronger way than it is the case for the single droplets. One can argue that the attractive force F between the islands is proportional to the sixth power of their radii, as demonstrated in (13). The intrinsic droplets in the strip undergo a maximum shrinkage, and they can coalesce when the polymer film between the water droplets is not large enough. If we have an extension of the water vapor comparable to the thickness of the polymer layer (about $4\,\mu m$), the total polymer solution will even move to the space in between the water droplets. As a consequence, there only remains a quite thin polymer film underneath the water droplets, such that the polymer solution will be uniformly distributed with respect to the AA* line. The subsequent evaporation of amyl acetate out of the solution does not give rise to an essential redistribution of the polymer relating to the AA* line. We end up with the result that the depth of the cell structure (i.e., its dilation in the third spatial dimension) shown in Fig. 3(b) is larger (about $1.5\,\mu m$) than the one displayed in Fig. 2 (about $0.5\,\mu m$). Moreover, they follow a stronger symmetry with respect to the AA* line.

Figures 2, 4, and 5 give rise to the assumption that, first, the solidification of the polymer network (i.e.,
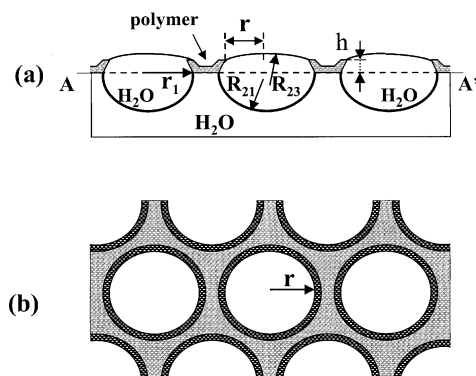

Fig. 6. Model structure of the network according to the experimental situation in Fig. 4: (a) shape of the cross-section of the interknot connection; (b) form of the network. r_1 is the radius of the deformed water droplets.

evaporation of amyl acetate) takes place, and afterwards the water droplet will break through the thin polymer film and flow into the cooled water (see the dark bursting holes within the cells of Fig. 4). As already noted above, the thickness of the liquid polymer layer is about $4\,\mu m$ after dissolving on the water surface. During the drying process, the thickness of the polymer layer amounts to about $0.5\,\mu m$. As can be clearly recognized in Figs. 2 and 5, the whole polymer material dissolved in amyl acetate is solidified in the AA* region, more precisely, above that line.

If the height h (see Fig. 5(b)) of the enveloping polymer layer is not too large, a hexagonal patterning can be achieved. The experimental realization is captured in Fig. 2, and the underlying basic cell structure is outlined in Figure 5(c). That means that, at a low height, also the width of the interknot connection will be small. The junctions cross in the knots of the hexagonal network under an angle of $120°$ and usually form a continuous network. Apparently, the hexagonal networks develop at small values of h, as a result of the cross-over of three types of zig-zag lines which proceed to the directions 1, 2, and 3 (see Fig. 5(c)). It must be emphasized that the hexagonal shape of the elementary cells of the polymer network becomes clearer during evaporation.

In case the water vapor begins to affect the nitrocellulose layer not until 60 s after spreading it onto the cooled water surface, the thin polymer film gradually becomes dry in the meantime. In other words, evaporation of amyl acetate out of the polymer layer during the elapsed time of 60 s gives rise to an increasing concentration of the polymer inside the polymer film.

As a consequence, the distance between neighboring droplets of water vapor that precipitate onto the liquid surface of the polymer layer increases ($\gamma_{Fl/G}$ is larger, see (13)). Accordingly, the same holds for the interspace between neighboring droplets of the water vapor, where the polymer material accumulates after the polymer thin film has completely become dry (in the vicinity of the AA* line). In this case, the cross-section of the interknot connection will have the shape of a plate (Fig. 6(a)), and the whole network resembles that one shown in Figure 6(b). The lifted edges in Fig. 6(a) are displayed together with the different pattern in Figure 6(b). Upon comparing the experimental results in Fig. 4 with the modelled networks in Fig. 6, one recognizes a good correspondence.

4. Nitrocellulose Networks as Precursor for Carbon Networks

Fabrication of self-organized precursory polymer network structures has been described in detail elsewhere (see Sect. 2.1). For obtaining carbon networks with different electrical conductivity, the cellulose precursor sample is annealed for two hours at process temperatures T_{ht} ranging from 500 to 1000 °C under vacuum conditions ($1 \cdot 10^{-5}$ mbar). As a result, we end up with carbon net structures that predominantly have hexagonal elementary cells with a diameter ranging from 1 to 3 μm (see Fig. 3(a)). The width of the interconnections depends on the diameter of the hexagonal cells of the carbon network and, thus, varies between 100 and 350 nm for different samples. The thickness of the interconnections in all samples is about 40 nm. For the sake of performing electrical measurements, four gold contacts were evaporated. The resulting active area of the carbon network fragment confined between the contacts was about 40 μm · 40 μm. In order to be able to reach the regime of linearity in the current-voltage characteristic by recording the dependence of the specific resistivity on temperature in the range from 4.2 to 295 K, the current varied from 0.1 nA (in the high ohmic regime) to 100 nA (in the low ohmic regime). The specific resistivity was calculated using the relation $\rho = Rs/L$; R is the resistance of the network (measured in the linear regime of the current-voltage characteristics), s the overall net cross-section, equal to the sum over all cross-sections of parts of the car-

bon network that are connected with the Au contacts, and L the length of the net, i.e., the distance between the Au contacts. Current-voltage characteristics have been recorded in the operation regime of the power source, each at constant temperature within the range from 4.2 to 290 K. In order to arrive at an as accurate as possible examination of the dependence of the conductivity on the electrical field, current-voltage measurements were carried out separately in the following electrical field regimes: 0 - 10 V/cm; 0 - 100 V/cm; 0 - 1000 V/cm, and 0 - 9000 V/cm.

4.1. Temperature Dependence of Hopping Transport in Carbon Networks

4.1.1. Experimental Temperature Dependence of the Specific Resistivity

In Fig. 7, the dependence of the specific resistivity on inverse temperature, $\rho(1/T)$, is shown in a semi-logarithmic plot for the samples 1 to 12. The corresponding annealing temperature T_{ht}, and also the relating specific resistivity at room temperature, ρ (295 K), taken for each annealing temperature, are given in Table 1. In contrast to our expectations, the increase of the annealing temperature of the starting cellulose net structures does not always lead to a higher electrical conductivity in the annealed carbon network. For example, the resistivity of a carbon net annealed at a temperature of 700 °C (curve 5) is by orders of magnitude lower than that for a net annealed at a temperature of 725 °C (curve 2). The latter phenomenon is more pronounced in the lower temperature range. The dependences of the specific resistivity on temperature displayed in Fig. 7 are characteristic for VRH, commonly described by (1). For obtaining an as precise as possible value of the characteristic parameter p, we turn to the local activation energy ε_a according to [5, 41, 42]:

$$\varepsilon_a = \frac{d(\ln \rho)}{d(1/k_B T)}, \qquad (14)$$

where k_B is the Boltzmann constant. Figure 8 shows a double-logarithmic plot of $\varepsilon_a(T)$, where four characteristic temperature ranges are indicated. A careful analysis of the dependence $\varepsilon_a(T)$ for each sample was carried out in Fig. 9, in order to determine the value of p and its corresponding temperature range. Upon decreasing the ambient temperature of the samples 8

Table 1. Electrical parameters of carbon networks investigated (samples No. 1 - 12). T_{ht} is the annealing temperature, $\rho(295\,K)$ the specific resistivity at 295 K, c the exponent in (5), which holds in the temperature range from T_c to T_b; α_b, α_M, and α_{CG} are the exponents of the local activation energy $\varepsilon_a(T) \propto T^\alpha$ in the temperature ranges from T_b to T_{13}, from T_{13} to T_{12}, and from T_{12} to 4.2 K, respectively; b and p_M are the exponents in (4), which hold in the temperature ranges from T_b to T_{13} and from T_{13} to T_{12}, respectively; p_{CG} is the exponent in (3), which holds in the temperature range from T_{12} to 4.2 K.

No.	T_{ht} °C	$\rho(295\,K)$ mΩcm	c	α_b	b	α_M	p_M	α_{CG}	p_{CG}	T_c K	T_B K	T_{13} K	T_{12} K
1	600	8360	–	–	–	0.61	2.56	–	–	–	–	295	–
2	725	200	–	1.10	3.13	–	–	0.48	1.92	–	295	–	90
3	775	56	–	1.06	1.97	–	–	0.44	1.78	–	295	–	85
4	775	35	–	1.00	1.20	0.66	2.94	0.44	1.78	–	295	140	75
5	700	28	–	0.91	0.80	0.57	2.32	0.38	1.61	–	295	135	55
6	750	20	–	0.94	0.62	0.63	2.70	0.40	1.66	–	295	120	40
7	800	15	–	0.98	0.48	0.62	2.63	0.33	1.49	–	295	85	15
8	950	12	1.43	0.91	0.33	0.64	2.78	–	–	295	150	18	4.2
9	900	10	1.32	0.97	0.08	–	–	–	–	295	17	4.2	–
10	1000	9	1.45	0.99	0.07	–	–	–	–	295	17	4.2	–
11	900	9	1.49	0.91	0.06	–	–	–	–	295	17	4.2	–
12	1000	8	1.41	1.06	0.04	–	–	–	–	295	17	4.2	–

Table 2. Parameters of VRH in the Coulomb gap of carbon networks investigated (samples No. 2 - 7). T_M and T_{CG} are constants in (4) for Mott's hopping law and in (3) for VRH in the Coulomb gap, respectively; ε_r is the dielectric constant, a the radius of the localized states, ΔE_{CG} the Coulomb gap width at $T = T_{12}$, $k_B T_{12}$ the thermal energy at $T = T_{12}$; ε_{optCG} is the optimum hopping energy in the Coulomb gap, ε_{optM} the optimum hopping energy in Mott's hopping law, ε_a the experimentally obtained local activation energy at $T = T_{12}$; ρ_0 and ρ_0^* are constants in (3) and (4), respectively; N_{0CG} is the density of states at the edge of the Coulomb gap.

No.	T_M K	T_{CG} K	ε_r	a nm	ΔE_{CG} meV	$k_B T_{12}$ meV	ε_{optCG} $T=T_{12}$ meV	ε_{optM} $T=T_{12}$ meV	ε_a $T=T_{12}$ meV	ρ_0^* mΩcm	ρ_0 mΩcm	N_{0CG} eV^{-1}cm^{-2}
2	–	3637	6	2	–	7.7	24.6	–	24.7	–	15	$5.4 \cdot 10^{13}$
3	–	1005	11	4	–	7.3	12.6	–	13.5	–	15	$9.4 \cdot 10^{13}$
4	5352	761	13	5	25.6	6.4	10.3	10.6	9.5	2.4	64	$1.1 \cdot 10^{14}$
5	2467	447	17	6	19.2	4.7	6.7	6.7	6.1	3.3	4.7	$1.2 \cdot 10^{14}$
6	869	180	29	10	8.8	3.4	3.6	3.8	3.4	6.2	11	$1.9 \cdot 10^{14}$
7	353	66	44	16	2.9	1.2	1.3	1.5	1.3	8.6	18	$1.6 \cdot 10^{14}$

to 12 from $T_c = 295$ K to T_b (Table 1), we recognize a rapid reduction of the local activation energy according to $\varepsilon_a(T) \propto T^\alpha$. The characteristic values $\alpha = c$ of these samples are also given in Table 1; they are about 1.3 to 1.5. Reducing the ambient temperature of the samples 2 to 12 from T_b to T_{13} leads to an overall dependence $\varepsilon_a(T) \propto T^\alpha$ with $\alpha = \alpha_b \approx 1.0$ (see Table 1). Even lower temperatures from T_{13} to 4.2 K cause a significant reduction of the dependence $\varepsilon_a(T)$. At temperatures varying from T_{13} to T_{12}, the exponent α is denoted by α_M, while in the temperature range from T_{12} to 4.2 K, α is denoted by α_{CG}. In Table 1, the corresponding numerical values of α_M and α_{CG} are listed. The values of α_M give rise to the assumption that the temperature dependence of the

specific resistivity from T_{13} to T_{12} can be described by Mott's hopping law for the two-dimensional case. For different samples, the mean value of α_M is 0.63. Upon further decreasing the temperature from T_{12} to 4.2 K, VRH in the Coulomb gap is observed. The values of α_{CG} diminish when approaching the MIT on the insulating side (see Table 1).

In Table 2, the values of T_0 introduced in (1) are given. They were extracted from the experimentally obtained dependences $\ln \rho \propto (T_0/T)^{1/p}$ for $p = 3$ and $p = 2$ in the corresponding temperature ranges and denoted by T_M and T_{CG}, respectively. In the inset of Fig. 9, the dependence of T_{CG} on T_M is plotted on a double-logarithmic scale for the samples showing both, Mott's hopping law and VRH in the Coulomb
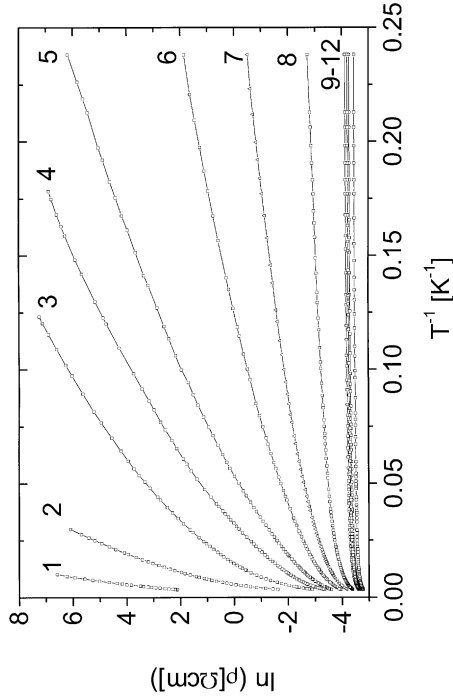
Fig. 7. Dependence of the specific resistivity of carbon nets on inverse temperature plotted on a semi-logarithmic scale. The numbers of the different samples are indicated, their annealing temperature can be found in Table 1.

Fig. 8. Dependence of the local activation energy on temperature, plotted on a double-logarithmic scale. The numbers of the curves correspond to the numbers in Figure 7. B gives the slope of the approximation line.
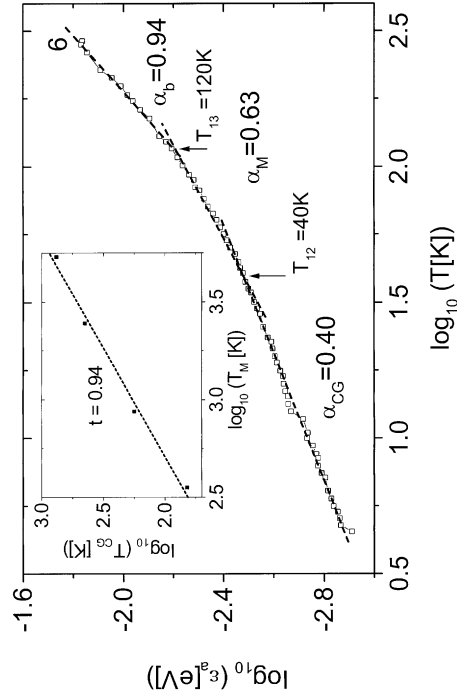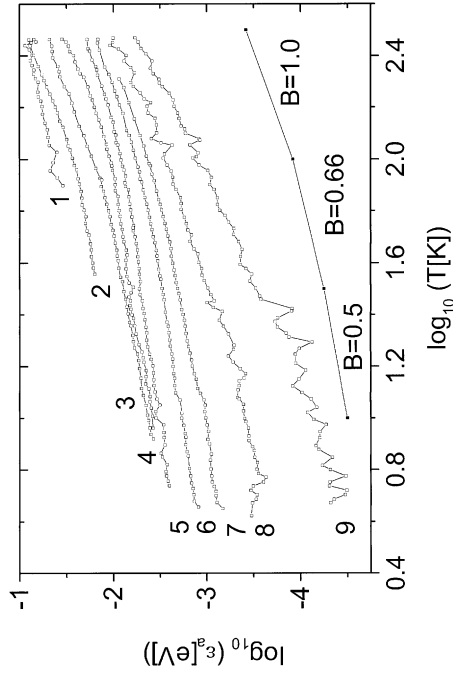
Fig. 9. Dependence of the local activation energy on temperature of sample 6, plotted on a double-logarithmic scale. The dashed lines give the approximation of the dependence $\varepsilon_a(T)$ in the corresponding temperature range. The inset shows the dependence $T_{CGt} = A T_M{}^t$ plotted on a double-logarithmic scale.
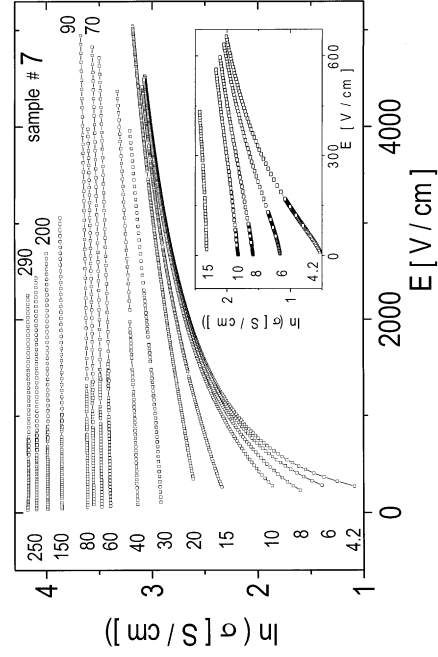
Fig. 10. Dependence of the conductivity on the electrical field of sample 7, taken at different temperatures (values indicated in K) and plotted in a semi-logarithmic scale. The inset magnifies the same dependence in the regime of lower electrical fields.

gap, in different temperature ranges. Obviously, the relationship between these two constants follows the phenomenological equation $T_{CG} = AT_{M}^{t}$ with $A \approx 0.07$ and $t \approx 1$.

As aforementioned, nearly all samples investigated disclose a temperature range where the exponent of the dependence $\varepsilon_a(T) \propto T^{\alpha}$ is $\alpha = \alpha_b \approx 1.0$ (see Table 1). That means that in the temperature range from T_b to T_{13} the dependence $\rho(T) \propto T^{-b}$ is observed. The values of b given in Table 1 were evaluated from the fits of the curves $\ln \rho(\ln T)$, experimentally obtained in the temperature range from T_b to T_{13}.

At this point, some experimental results should be discussed in detail. For the samples 2 and 3, it is not that easy to specify exactly the range of the dependence $\varepsilon_a \propto T^{\alpha}$, where Mott's hopping law holds. The latter range becomes more evident for the case of sample 4. In contrast, Mott's hopping law could even be observed for the whole temperature range from 80 to 295 K in sample 1.

4.1.2. Analysis of the Specific Resistivity

In connection with the above analysis of the temperature dependence of the local activation energy $\varepsilon_a(T)$, all dependences $\rho(T)$ of the carbon networks in the temperature range from 4.2 to 295 K could be represented analytically as the sum of four laws [43, 44]. The first one describes the VRH in the Coulomb gap at temperatures varying from 4.2 K to T_{12}, according to

$$\rho(T) = \rho_0 \, \exp \left(\left[\frac{T_{CG}}{T} \right]^{(1/p_{CG})} \right). \tag{15}$$

The second and the third law characterize the VRH with a constant density of localized states in the temperature range from T_{12} to T_{13} and the power law of $\rho(T)$ in the temperature range from T_{13} to T_b for all samples, respectively. Analytically, they can be written as

$$\rho(T) = \rho_0^* \, T^{-b} \, \exp \left(\left[\frac{T_M}{T} \right]^{(1/p_M)} \right). \tag{16}$$

Take note of the fact that the dependence $\rho(T) \propto T^{-b}$ in (16) strongly dominates the transport behavior of all samples in the temperature range from T_{13} to T_b. In case of a low share of Mott's hopping law at temperatures ranging from T_{12} to T_{13} (samples 2 and 3), the exponential part in (16) is negligible. The

fourth law characterizes the temperature range from T_b to T_c according to

$$\rho(T) = \rho_1 \, \exp \left(- \left[\frac{T}{T_1} \right]^{c-1} \right). \tag{17}$$

The parameters b, c, p_{CG}, p_M, ρ_0, ρ_0^*, ρ_1, T_{CG}, T_M, and T_1 in the above equations are constants. For all samples far from the MIT, (15) and (16) dominate the dependence $\rho(T)$ (see Table 1). Simultaneously, (17) and the power law part in (16) become more important for samples near the MIT. The temperature dependence of the specific resistivity of sample 8 represents some kind of threshold between the dependences $\rho(T)$ near and far from the MIT. For the samples 8 to 12, the values of T_1 in (17) amount to 320, 1290, 1880, 1980, and 3190 K, respectively. The corresponding values ρ_1 are calculated to be 21, 17, 16, 15, and 13 mΩcm, respectively.

Following (14) and (15), the temperature dependence of the local activation energy in the range from 4.2 K to T_{12}, where VRH in the Coulomb gap is observed, can be described by

$$\varepsilon_a(T) = k_B(1/p_{CG})T_{CG}^{(1/p_{CG})}T^{(1-(1/p_{CG}))}. \tag{18}$$

For temperatures ranging from T_{12} to T_b, the local activation energy is given by

$$\varepsilon_a(T) = k_B bT + k_B(1/p_M)T_M^{(1/p_M)}T^{(1-(1/p_M))}. \tag{19}$$

The second term characterizes the dependence $\varepsilon_a(T)$ for temperatures varying from T_{12} to T_{13}, the first term from T_{13} to T_b. In the temperature range from T_b to T_c, the dependence $\varepsilon_a(T)$ reads

$$\varepsilon_a(T) = (c-1)k_B T \left(\left[\frac{T}{T_1} \right]^{c-1} \right). \tag{20}$$

A double-logarithmic plot of $\varepsilon_a(T)$, e. g., for sample 6, is shown in Figure 9. Therefrom, the values of the parameters p_{CG} and p_M in the corresponding temperature ranges could be obtained. Following (18), the characteristic value p_{CG} of (15) in the temperature range from 4.2 K to T_{12} is $p_{CG} = 1/(1 - \alpha_{CG})$. By approaching the MIT on the insulating side, the characteristic value p_{CG} decreases (see Table 1). From Eq. (19) follows that the characteristic value p_M in the temperature range from T_{12} to T_{13} is $p_M = 1/(1 - \alpha_M)$.

For different samples, the mean value of p_M in (16) is about 2.7.

4.1.3. Coulomb Gap

The appearance of the Coulomb gap in the density of states near the Fermi energy derives from the Coulomb interaction of charge carriers localized at different impurity centers [3 - 5]. The transition from the ES law to Mott's hopping law at the temperature T_{12} can be explained as follows. The charge carriers at $T > T_{12}$ move via states that are located outside the Coulomb gap, where the density of localized states is only weakly dependent on energy. The presence of both, Mott's hopping law and the VRH in the Coulomb gap for the samples 4 to 7, indicates that the impurity band width of these samples is much higher than the Coulomb gap width. For the samples 2 and 3, Mott's hopping law is only weakly present. Hence, one can conclude that the density of localized states outside the Coulomb gap is not constant.

From the values given in Tables 1 and 2, the change in the Coulomb gap width by approaching the MIT on the insulating side can be determined. Following [5], the expressions for calculating the constant T_0 in (1) with $p = 3$ and $p = 2$ are

$$T_M = \frac{\beta_M}{k_B a^2 N_0} \tag{21}$$

and

$$T_{CG} = \frac{\beta_{CG} e^2}{k_B a \varepsilon_r}, \tag{22}$$

respectively, where a means the radius of the localized states, N_0 the constant density of states outside the Coulomb gap, and ε_r the dielectric constant. According to [5], we have $\beta_M = 13.8$ and $\beta_{CG} = 2.8$. The dependence of the density of localized states on energy in the vicinity of the Coulomb gap for 2D is

$$N_{CG}(E) = \frac{\lambda \varepsilon_r^2 |E - E_F|}{e^4} \tag{23}$$

with $\lambda = 2/\pi$. From (21), (22), and (23) follows that the Coulomb gap width at $T = T_{12}$ can be expressed as

$$\Delta E_{CG} = \frac{\beta_M k_B T_{CG}^2}{\lambda \beta_{CG}^2 T_M}. \tag{24}$$

For the samples 4 to 7, we can obtain the values of the Coulomb gap width at $T = T_{12}$ by substituting the values T_{CG} and T_M (received from measurement, see Table 2) in (24).

In addition, the Coulomb gap width can also be determined by the value of the optimum hopping energy in the Coulomb gap, ε_{optCG}. Its temperature dependence is given by [5, 45]

$$\varepsilon_{optCG} = A_{CG} k_B (T_{CG} T)^{1/2} \tag{25}$$

with $A_{CG} = 0.5$. For energy values lying outside the Coulomb gap, where Mott's hopping law applies, the temperature dependence of the optimum hopping energy for 2D can be described by [5]

$$\varepsilon_{optM} = A_M k_B (T_M T^2)^{1/3} \tag{26}$$

with $A_M = \beta_M^{-1/3} = 0.4$.

In Table 2, the values of these optimum hopping energies at the temperature T_{12} calculated from both sides, the Coulomb gap side, (25), and the side of a constant density of states N_0, (26), are given. The values of the local activation energy ε_a at $T = T_{12}$, experimentally obtained from the dependences $\varepsilon_a(T)$ (see Figs. 8, 9), are also shown in Table 2. A good correlation between these three parameters can be observed by comparing them. According to [5], the Coulomb gap width ΔE_{CG} is twice as big as those of the optimum hopping energy ε_{optCG}, in agreement with our results in Table 2. The absolute values of the Coulomb gap width at the temperature T_{12} obtained in a different way are in good accordance with each other – certainly a proof for the reliability of these values. Comparing the values of ε_{optCG} and $k_B T_{12}$, one can see that, far from the MIT, the optimum hopping energy in the Coulomb gap is much higher than the energy $k_B T_{12}$. The more one approaches from the insulating side of the MIT, the smaller becomes the difference between these two values. One can conclude that the optimum hopping energy at $T \leq T_{12}$ is smaller than the Coulomb gap width and, therefore, the ES law is observed in the experiment at $T \leq T_{12}$, (15). On the other hand, the optimum hopping energy at $T > T_{12}$ is larger than the Coulomb gap width. The latter means that Mott's hopping law with a constant density of states, N_0, is dominant. Equating the value of $2\varepsilon_{optCG}$ with the one of the Coulomb gap width, the value of N_0 at the edge of the Coulomb gap can be calculated from (23). In Table 2, such values of N_0 are listed and denoted as N_{0CG}. It can be seen that the density of states near the Fermi energy enlarges by a factor

Table 3. Parameters of Mott's hopping law of carbon networks investigated (samples No. 4 - 8). $k_B T_{13}$ and $k_B T_h$ are the thermal energies at $T = T_{13}$ and $T = T_h$, respectively; T_h is the intermediate point of the temperature range from T_{12} to T_{13}; $\varepsilon_{\mathrm{optM}}$ is the optimum hopping energy in Mott's hopping law, ε_a the experimentally obtained local activation energy, N_{0M} the density of states in Mott's hopping law.

No.	$k_B T_{13}$/meV	$\varepsilon_{\mathrm{optM}}$/meV $T = T_{13}$	ε_a/meV $T = T_{13}$	T_h/K	$k_B T_h$/meV	$\varepsilon_{\mathrm{optM}}$/meV $T = T_h$	ε_a/meV $T = T_h$	N_{0M}/eV^{-1}cm^{-2}
4	12.1	16.1	14.2	107	9.2	13.4	11.7	$1.2 \cdot 10^{14}$
5	11.6	12.1	10.0	95	8.2	9.6	8.0	$1.8 \cdot 10^{14}$
6	10.3	7.9	6.7	90	7.7	6.6	5.2	$1.8 \cdot 10^{14}$
7	7.3	4.7	3.7	50	4.3	3.3	2.6	$1.8 \cdot 10^{14}$
8	1.5	0.68	0.5	10	0.86	0.46	0.4	–

of three during the transition from sample 2 to sample 7. Moreover, the values of the density of localized states, N_{0M}, resulting from (21) in the validity range of Mott's hopping law (Table 3), are nearly the same as those of N_{0CG}, resulting from (11) at the edge of the Coulomb gap (Table 2). Such accordance of N_{0M} and N_{0CG} at the transition point, T_{12}, again suggests a proof for the reliability of these values.

Resulting from (23), the Coulomb gap width for $T = T_{12}$ depends on the density of states at the edge of the Coulomb gap, N_{0CG}, and the dielectric constant ε_r. The decrease of the Coulomb gap width by approaching the MIT on the insulating side until its closure is mainly a consequence of the increase of the dielectric constant ε_r and its divergence at the MIT ($\varepsilon_r \to \infty$) [46, 47]. So the decrease and closure of the Coulomb gap by approaching the MIT on the insulating side lead to a lowering of the critical temperature T_{12} (see Table 1) and the constant T_{CG} (see Table 2). Furthermore, the decrease of T_{12} and T_{CG} also depends on the localization length by approaching the MIT on the insulating side.

As already mentioned above, a lowering of the value of p_{CG} in (15) by approaching the MIT on the insulating side was observed. One reason for such a decrease might be related to the transformation of the form of the Coulomb gap, (23), the latter becoming steeper at lower energies, e. g., $N(E) \propto E^{3/2}$ (see [48]).

4.1.4. Hopping Energy in the Validity Range of Mott's Law

In Table 3, the parameter values of the optimum hopping energy in Mott's law, $\varepsilon_{\mathrm{optM}}$, (26), the experimentally obtained local activation energy ε_a, and the thermal energy $k_B T_{13}$ at $T = T_{13}$, i. e., at the upper edge of the validity range of Mott's hopping law, are

listed. For the samples 4 and 5, the values of $\varepsilon_{\mathrm{optM}}$ and ε_a are either higher or comparable to the values of $k_B T_{13}$. The values of $k_B T_{13}$ become larger than that of $\varepsilon_{\mathrm{optM}}$ and ε_a, starting at sample 6. Such tendency also holds at the intermediate point T_h of the temperature range from T_{12} to T_{13} (Table 3). For all samples where Mott's hopping law is observed, the overtop of the parameters $\varepsilon_{\mathrm{optM}}$ and ε_a over the values of $k_B T$ is only valid near the temperature T_{12}. Too small values of the parameters $\varepsilon_{\mathrm{optM}}$ and ε_a in relation to $k_B T$ in the temperature range from T_{12} to T_{13} could be explained by the influence of the pre-exponential part $\rho(T) \propto T^{-b}$ on the exponential part in (16). This influence is particularly important close to the temperature $T = T_{13}$. Indeed, a more strongly pronounced dependence $\varepsilon_a \sim T^{1.0}$ at temperatures $T \approx T_{13}$ compared to the dependence $\varepsilon_a \sim T^{2/3}$ (Fig. 9) diminishes the experimentally obtained values of ε_a.

4.1.5. Radius of the Localized States

For the determination of the radius of the localized states, the value of the dielectric constant ε_r of the carbon networks we have investigated has to be well known. Resulting from the inset of Fig. 9, the phenomenological equation is $T_{CG} = A T_M{}^t$ with $A \approx 0.07$ and $t \approx 1$. Furthermore, the correlations $T_M \propto 1/a^2$ and $T_{CG} \propto 1/a\varepsilon_r$ are a direct consequence of (21) and (22), respectively. Upon comparing these correlations with the experimental data, we find $T_M/T_{CG} \propto \varepsilon_r/a \to$ const or $\varepsilon_r \propto a$. That means that the critical exponent for both ε_r and a by approaching the MIT on the insulating side is nearly the same. Our result agrees well with experimental data of amorphous Cr-SiO$_x$ thin films [49] and indium doped CdSe crystals [50]. We have compared our values of T_{CG} for sample 2, furthermost situated from the MIT, with the values of carbon fibers [51]

and come to the conclusion that the value of the dielectric constant for sample 2 is $\varepsilon_r = 6$. By using the correlations $T_{CG} \propto 1/a\varepsilon_r$ and $\varepsilon_r \propto a$, the change of ε_r differing from sample to sample can be calculated. In Table 2, such values of ε_r for the samples 2 to 7 are listed. The radii of the localized states, a, can be determined from the resulting experimental data of T_{CG} and (22), also given in Table 2.

4.1.6. High-temperature Conductivity

Next, we analyze in detail the temperature ranges from T_{13} to T_b and from T_b to T_c, where the phenomenological correlation $\rho(T) \propto T^{-b}$ and (17) are valid. In the whole temperature range investigated we did not find hopping with a constant activation energy for any of the samples mentioned. That means, there is no hopping between nearest-neighbor localized states at temperatures varying from 4.2 to 295 K. Therefrom one can suppose that in our porous carbon networks tails of localized states pulled out of the conduction and valence band as a result of disorder and some overlap between these tails occur [1, 52]. The nearer the states are situated to the mobility edge, the weaker they are localized. The mobility edge is defined as an energy threshold which separates localized states from delocalized ones [52]. At high temperatures (from T_{13} to T_b), tunneling of the charge carriers occurs via weakly localized states at the smallest barriers. The influence of the dependence $\rho(T) \propto T^{-b}$ ($b \to 0$) decreases and shifts to lower temperatures at the samples 8 to 12 that are near the MIT. The latter phenomenon is closely connected with the existence of the temperature range from T_b to T_c, where the dependence of $\rho(T)$ follows (17). Such stronger dependence of $\rho(T)$ possibly derives from the transfer of the charge carriers excited at the mobility edge.

4.2. Electrical Field Dependence of Hopping Transport in Carbon Networks

4.2.1. Experimental Field Dependence of the Conductivity

In Fig. 10, typical conductivity versus electrical field characteristics of sample 7 recorded at different values of the ambient temperature (from 4.2 up to 290 K) are displayed in a semi-logarithmic representation [53]. The same functional dependences can be also obtained for the case of sample 6 (not shown here). In the inset of Fig. 10 we have plotted a blow-up

of the conductivity versus electrical field characteristic of sample 7 in the low-field regime. Obviously, a linear dependence between the conductivity and the electrical field strength (i. e., the horizontal parts of the curves in the semi-logarithmic representation of Fig. 10) is present only in the limited field interval indicated on the r.h.s. of the characteristics. Upon decreasing the temperature, the extension of that field range noticeably decreases. A still more accurate determination of characteristic changes in the dependence $\sigma(E)$ at constant temperature can be achieved via analyzing the modifications in the slope of the curves $\sigma(E)$. It is, therefore, helpful to use the parameter [43]

$$w_\sigma(E) = \mathrm{d} \ln \sigma(E) \,/\, \mathrm{d}\, E, \qquad (27)$$

which denotes nothing but a measure of the degree of nonlinearity in the conductivity versus electrical field characteristic. At constant temperature, (2) can be expressed as

$$\sigma(E) = \sigma(0) \exp\left(AE^n\right). \qquad (28)$$

Here, the constants $\sigma(0)$ and A are functions of temperature, but they do not depend on the electrical field. The parameter w_σ is then given by

$$w_\sigma(E) = A\,n\,E^{n-1}. \qquad (29)$$

We emphasize that the case $n = 0$ means saturation of the conductivity, i.e., $\sigma = $ const.

The exponent n in Eq. (28) can be gained from plotting the experimental data of the dependence $\log w_\sigma$ versus $\log E$ and taking advantage of the slope of the approximation line. In Fig. 11, the electrical field dependence of the parameter w_σ for the $\sigma(E)$ curves of sample 7 (Fig. 10) is displayed in a double-logarithmic scale. The different ambient temperatures distinguishing the curves correspond to that in Figure 10. For the sake of a vivid illustration of the experimental results, we have also marked in Fig. 11 the slope of the curve that corresponds to the value $n = 1$. It becomes obvious that, within the low electrical field range, (28) with $n = 1$ is valid. For each curve in Fig. 11, the end of the latter regime is always indicated by an arrow. With increasing temperature, the validity range of $n = 1$ clearly shifts towards the regime of higher electrical fields. For temperatures $T \geq 70$ K, the $n = 1$ interval was not at all attainable within the scope of field strength applied by us.
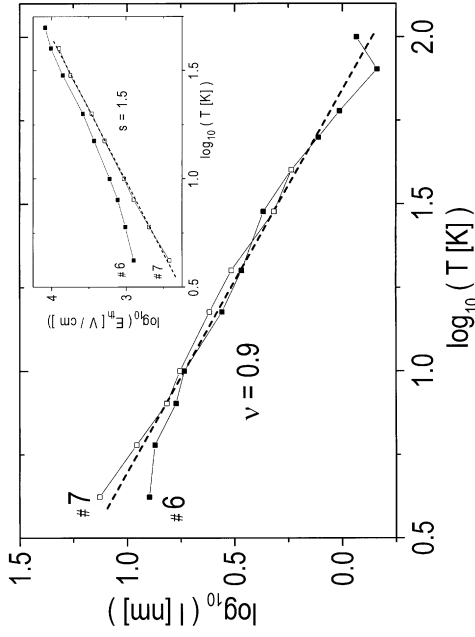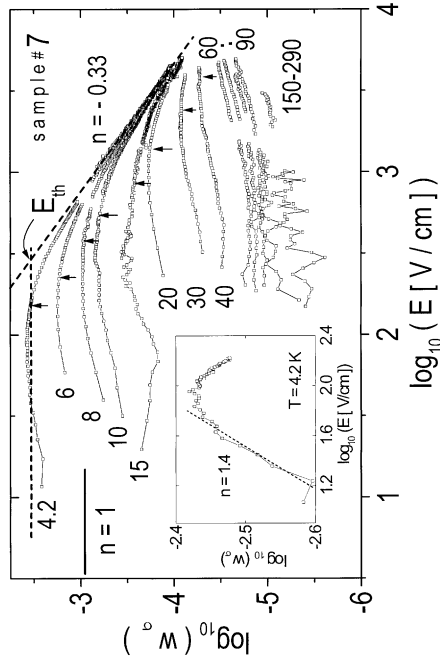
Fig. 11. Dependence of the parameter w_σ, (27), on the electrical field of sample 7, taken at different temperatures (values indicated in K) and plotted in a double-logarithmic scale. The data are extracted from the $\sigma(E)$ curves of Figure 10. E_{th} is the characteristic threshold electrical field, defining the transition from the low to the high field regime. In practice, the intersection of the corresponding approximation lines (the slope of which is nothing but the exponent n of (28)) is referred to as E_{th}. The upper limit of the low field interval, where $n = 1$ ceases to be valid, is marked by an arrow. The inset focusses on the dependence $w_\sigma(E)$ at the temperature $T = 4.2$ K and lower electrical fields.
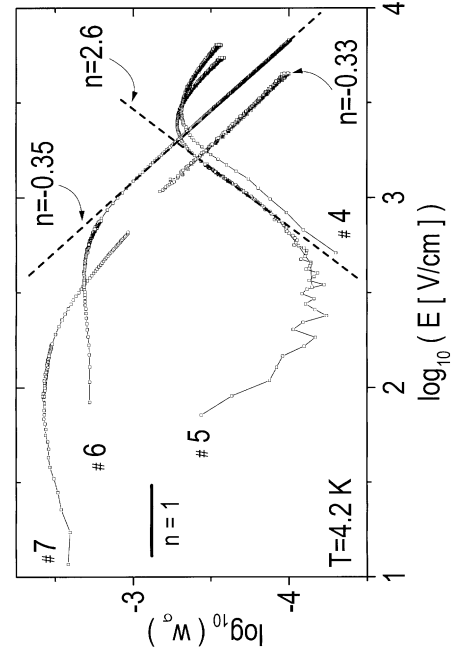

Fig. 12. Dependence of the hopping length on temperature of the samples 6 and 7, plotted in a double-logarithmic scale. The inset displays the temperature dependence of the characteristic threshold electrical field E_{th}. The exponents ν and s of the relations $l \propto T^{-\nu}$ and $E_{th} \propto T^s$, respectively, can be immediately drawn from the experimental data.

Fig. 13. Dependence of the parameter w_σ, (27), on the electrical field of the samples 4, 5, 6, and 7, taken at the temperature $T = 4.2$ K and plotted in a double-logarithmic scale. According to Fig. 11, the total electrical field regime analyzed divides into intervals of different slopes of the $w_\sigma(E)$ curves, i.e., different values of the exponent n of (28).
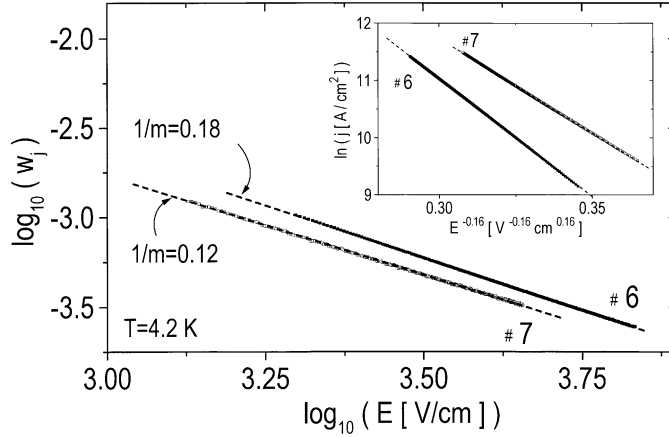
Fig. 14. Dependence of the parameter w_j, (30), on the electrical field of the samples 6 and 7, taken at the temperature $T = 4.2$ K and plotted in a double-logarithmic scale. The inset shows the dependence of the current density on the electrical field, taken at the temperature $T = 4.2$ K and plotted in a semi-logarithmic scale. The exponent $1/m$ of (3) can be immediately drawn from the experimental data (in analogy to the determination of the exponent n of (28) in Fig. 13).

Upon closer looking at the inset of Fig. 11 (blow-up of the 4.2 K curve in the low electrical field range), we uncover an interval where (28) with $n = 1.4$ is valid that precedes the $n = 1$ part of the curve. The $n = 1.4$ interval also extends to the high field range with increasing temperature. The apparent saturation of the conductivity versus electrical field characteristics ($n = 0$) and their subsequent complete merging into one curve ($n < 0$) are strongly pronounced in the functional dependence $w_\sigma(E)$, where the curves consolidate with the slope $n = -0.35$ (sample 6) and $n = -0.33$ (sample 7) – the latter case indicated in Figure 11. There exists a characteristic threshold electrical field (E_{th}) during the transition from the low to the high field range. For the case of sample 7 (see Fig. 11), the intersection point of the two approximation lines of the relationship $w_\sigma(E)$ between the interval of $n = 1$ and that of $n = -0.33$ was determined and marked by E_{th}.

After a rather comprehensive determination of the electrical field interval from the dependence $w_\sigma(E)$, where (28) with $n = 1$ applies and, thus, the parameter A in (28) is given by $A = C\,e\,r_m/k_BT = e\,l/k_BT$ (via (2) with $l = Cr_m$), the parameter l can be extracted. As already stated in the introductory part of the present paper, the parameter l is proportional to the maximum hopping length r_m. Hereto, the slope of the dependence $\ln\,\sigma(E)$ in the electrical field range governed by $n = 1$ was taken, and the value of l could be calculated for different temperatures. The resulting temperature dependence of the hopping length, $l(T)$, becomes evident in Fig. 12 for the case of the samples 6 and 7. Obviously, we end up with the law $l \propto T^{-\nu}$, where $\nu = 0.9$. In the inset of Fig. 12, the dependence of the threshold electrical field E_{th} on

temperature T is plotted in a double-logarithmic scale for the case of the samples 6 and 7. One plainly finds that the threshold increases with increasing temperature, following the law $E_{th} \propto T^s$, where $s = 1.5$.

Next, for comparison, we will analyze the dependences $\sigma(E)$ obtained experimentally at $T = 4.2$ K for the samples 4 - 7. The change of the character of $\sigma(E)$ can still be read off more vividly from the functional dependence $w_\sigma(E)$, as strongly manifested in Fig. 13 for $T = 4.2$ K. It must be emphasized that the value of the threshold electrical field E_{th} appreciably shifts to the higher field range, when increasing the distance from the MIT on the insulating side. Since the interval of the dependence $\sigma(E)$ with $n = 1$ is extremely small for the case of the samples 4 and 5, the relation $l(T)$ could not be gained with sufficient accuracy. Keep note of the fact that, for the samples 4 and 5, the field range that precedes the interval with $n = 1$, see (28), excels by a larger slope, i.e., $n = 2.6$. The low electrical field regime that precedes the interval with $n = 2.6$ could not be examined with sufficient accuracy for the case of the samples 4 and 5, as a consequence of inevitable large fluctuations in the dependence $w_\sigma(E)$.

In the low-temperature range at electrical field values $E \geq 2 \times 10^3$ V/cm, the conductivity does not depend on temperature for the case of the samples 6 and 7. In the above field regime described by (3), usually the dependence $j(E)$ is analyzed. A more accurate value of the parameter m can be obtained in analogy to the determination of the characteristic value n in (28), as described above. Therefore, the parameter $w_j(E)$ that features the nonlinearity of the dependence $j(E)$ is introduced and accordingly defined by

$$w_j(E) = \mathrm{d} \ln j(E) / \mathrm{d} E. \qquad (30)$$

We point out that our method for determining $1/m$ was already applied in [14]. Figure 14 displays the resulting dependences $w_j(E)$ at $T = 4.2$ K in a double-logarithmic scale. The values $1/m$ for the case of the samples 6 and 7, both extracted from the slope of the above dependence, amounted to 0.18 and 0.12, respectively. On the basis of the obtained average value $1/m = 0.16$, the dependence $\ln j$ versus $E^{-0.16}$ is plotted in the inset of Figure 14. An ideal straightening of $\ln j(E)$ in those coordinates can be clearly seen.

4.2.2. Analysis of the Conductivity

The linear relation between the logarithm of the conductivity and the electrical field at low temperatures that applies for samples near the MIT (i.e., samples 6 and 7) is present only in a relatively short field range. With increasing temperature, the above range extends to the high field regime. Such an enlargement of the region, where the linear $\sigma(E)$ characteristic dominates, can be explained by (2). At low temperatures, the exponential part in (2) is large, and its influence on the dependence $\sigma(E, T)$ becomes already apparent in the low electrical field range, compared to the pre-exponential part $\sigma(0)$. Upon increasing the temperature, the exponential part in (2) diminishes and comes into play only in the high electrical field range.

In the following, let us more accurately analyze the low electrical field range via (2). From the temperature dependence of the hopping length, $l(T)$, of the samples 6 and 7 plotted in Fig. 12, we obtain the law $l = C\, r_m \propto T^{-\nu}$, where $\nu = 0.9$, i.e., l increases with decreasing T. Note that for both samples the dependence $l(T)$ unveils two characteristic temperature regimes. First, in the range from 4.2 to 15 K, we have hopping conductivity in the Coulomb gap with $p_{CG} = 1.49$, see sample 7 in Table 1. In the temperature range from 15 to 85 K, we observe Mott's hopping law for the 2D case with $p_M = 2.63$. In the range from 4.2 to 40 K, the characteristic value $p_{CG} = 1.66$ was determined for sample 6. The interval with $p_M = 2.70$ embraces temperatures between 40 and 120 K. For the ensuing discussion, we use as appropriate values $p_{CG} = 2$ for VRH in the Coulomb gap and $p_M = 3$ for Mott's hopping law in case of all samples investigated. Following the experimentally gained dependence $l(T)$ shown in Fig. 12, it is difficult to detect

the difference between the dependence valid for hopping conductivity in the Coulomb gap and that for Mott's hopping law. According to [5 - 7], in the range of validity of (1) with $1/p = 1/2$ (or $1/p = 1/3$), the parameter l should increase with decreasing temperature proportional to $T^{-1/2}$ (or $T^{-1/3}$, respectively). However, the dependence obtained experimentally tells us that we have a much stronger rise of l during the reduction in temperature. A similar result has also been found in [18, 54]. It can only be explained under the assumption that the constant C increases with decreasing temperature. The change of the value of the constant C upon varying the parameter ξ_c (defined above as percolation threshold $\xi_c = (T_o/T)^{1/p}$) was predicted theoretically in [10, 55, 56]. Following [56], that modification in the range $16 \leq \xi_c \leq 29$ investigated is described by

$$C(\xi_c) = (14 \pm 2) \cdot 10^{-3}\, \xi_c. \qquad (31)$$

For the temperature range of Fig. 12, where (1) with $p = 2$ and $p = 3$ applies, the values of the parameter ξ_c are limited within the interval $2 \leq \xi_c \leq 6$. If one assumes that (31) also holds in the range of the parameter ξ_c investigated by us, then the dependence $l(T)$ can be expressed by

$$l = C\, r_m = A_c\, a\, \xi_c^2, \qquad (32)$$

where A_c is a constant. The maximum hopping length r_m and the localization radius a were already introduced in the frame of the discussion of (2). Now the dependence $l(T)$ in the temperature range, where hopping conductivity in the Coulomb gap (furtheron marked by the subscript CG) with $p = 2$ in (1) is present, looks like

$$l_{CG}(T) = A_c\, a\, T_{CG} / T. \qquad (33)$$

At temperatures where Mott's hopping law (furtheron marked by the index M) with $p = 3$ is present, the dependence $l(T)$ can be described as

$$l_M(T) = A_c\, a\, (T_M/T)^{2/3}. \qquad (34)$$

When comparing the analytically determined values of the dependence $l(T)$ in (33) and (34) with the experimentally gained ones in Fig. 12, good agreement can be observed. It should be emphasized that the intervals governed by the dependence $l_{CG}(T) \propto T^{-1}$

and the dependence $l_M(T) \propto T^{-2/3}$ of the experimental curves do not differ practically. A possible reason can be derived from the shortness of the temperature ranges, where the above dependences have been examined experimentally.

4.2.3. Threshold Electrical Field

As already mentioned in the experimental part of this work, the conductivity of the samples 6 and 7 near the MIT on the insulating side does not depend on temperature at electrical fields $E \geq 2 \times 10^3$ V/cm in the low-temperature range. The threshold electrical field E_{th} serves as a parameter that characterizes the transition from thermally activated to activationless hopping conductivity. Shklovskii [11] has deduced theoretically the relation $E_{th} \approx k_B T/ea$, which points at a dependence on temperature like $E_{th} \propto T^{1.0}$. Except to an accuracy of the numerical coefficient, the latter relationship applies both to the cases $p = 2$ and $p = 3$ in (1). The temperature dependence we have obtained for the samples 6 and 7 is of the form $E_{th} \propto T^{1.5}$ (see inset of Fig. 12). Such deviation can be explained by the following argument. In a relatively high electrical field, where the change of the potential energy of an electron, $eEl(T)$, along the hopping length $l(T)$ is equal to the extension of the energy range near the Fermi level, $\varepsilon_{opt}(T)$, that allows for hopping (i. e., the "optimum" hopping energy), the electron can move into the direction of the field. The hopping energy in the Coulomb gap had been expressed by (25). Equating the energies $\varepsilon_{optCG}(T)$ and $eE_{thCG}l_{CG}(T)$, where $\varepsilon_{optCG}(T)$ and $l_{CG}(T)$ are expressed by (25) and (33), respectively, results in a relation for the temperature dependence of the threshold electrical field in the Coulomb gap as

$$E_{thCG} = (A_{CG}\,k_B/\,A_c\,e\,a\,T_{CG}^{1/2})T^{3/2}. \quad (35)$$

Outside the Coulomb gap, i. e., in the range of validity of Mott's hopping law, the temperature dependence of the optimum hopping energy for the 2D case had been expressed by (26). Thus, the temperature dependence of the threshold electrical field outside the Coulomb gap can be written as

$$E_{thM} = (A_M\,k_B\,/\,A_c\,e\,a\,T_M^{1/3})T^{4/3}. \quad (36)$$

When comparing the analytical relations (35) and (36) with the dependences obtained experimentally,

a good correlation can be observed (see inset of Fig. 12).

The radii of the localized states, a, for the case of the samples 6 and 7 have been determined from the dependence $\sigma(1/T)$ in Section 4.1.5. Their values amounted to 10 and 16 nm (see Table 2), respectively. The value of a can also be gained from the analytical relations (33) or (34) and the slope of the experimental dependences $l(T)$, plotted in a double-logarithmic scale, see Figure 12. A similar analysis is possible with the help of the analytical equations (35) or (36) and the slope of the experimental dependences $E_{th}(T)$, see inset of Figure 12. Comparing the received values of a with the ones from Table 2 shows that the numerical characteristic value of $C(\xi_c)/\xi_c$ in (31) should be equal to 0.07 in the examined parameter interval $2 \leq \xi_c \leq 6$ (instead of the theoretical value [56] 0.014).

From (35) and (36), it follows that E_{thCG} and E_{thM} with increasing temperature shift to the high electrical field range. Such behavior can clearly be seen in the experimental dependences of Figure 11. The increase of E_{th} with temperature simultaneously leads to an extension of the low electrical field range, where (28) with $n = 1$ is valid, towards higher fields. The corresponding shift of the arrows in Fig. 11 provides direct experimental evidence.

The shift of the threshold electrical field E_{thCG} into the high field range with increasing distance from the MIT (i.e., turning from sample 7 via sample 6 and sample 5 to sample 4) at the temperature $T = 4.2$ K (see Fig. 13) mainly results from the rise of the parameter T_{CG}. From the equality of the energies $\varepsilon_{optCG}(T)$ and $eE_{thCG}l_{CG}(T)$, we end up with the relation $E_{thCG} \propto T_{CG}^{1/2}/l_{CG}$ for constant temperature. With increasing distance from the MIT on the insulating side, the parameter $T_{CG} \propto 1/a\varepsilon_r$ increases, as a consequence of the reduction of both the radius of localized states, a, and the dielectric constant ε_r. Such a conclusion can also be confirmed experimentally. For example, the values of E_{thCG} at $T = 4.2$ K for the samples 7 and 6 (see Fig. 13) amount to 260 V/cm and 790 V/cm, respectively. That means that, when turning from sample 7 to sample 6, we have a three-fold enlargement of the threshold electrical field. The value of T_{CG} becomes larger by approximately the same factor, i.e., $T_{CG} = 66$ K for the case of sample 7 and $T_{CG} = 180$ K for the case of sample 6 (see Table 2).

4.2.4. High and Low Electrical Field Ranges

In the experimental part of our work, it turned out that the electrical field range with $n > 1$ (exponent $n = 1.4$ for the samples 7 and 6) precedes the one with $n = 1$ in (28). With increasing temperature, also the range with $n > 1$ shifts to higher fields (see Fig. 11). Upon growing distance from the MIT on the insulating side at $T = 4.2$ K, for the samples 5 and 4, we observe both the shift of the interval with $n > 1$ to the high field range and the increase of the characteristic value of the exponent n up to $n = 2.6$ (see Fig. 13). We are familiar with only one work [8], where it is pointed out that the dependence $\ln \sigma(E)$ possesses a range of validity of the law $\ln \sigma(E) \propto E^2$. The latter should precede the range with the dependence $\ln \sigma(E) \propto E$.

Within the regime of high electrical fields and low temperatures, a saturation of the curves $\sigma(E) \propto E^n$ takes place together with a fusion to one curve (see Fig. 10). It can be clearly seen by the functional dependences $w_\sigma(E)$ (Fig. 13), where the curves with the slope $n = -0.35$ (sample 6) and the curves with $n = -0.33$ (sample 7) merge. In case of VRH, following Mott's hopping law for 3D in the high electrical field range, the relation $\ln \sigma(E) \propto E^{-1/4}$ was determined in the theoretical work of Apsley and Hughes [8]. It were straightforward to assume that the relation $\ln \sigma(E) \propto E^{-1/2}$ applies for VRH in the Coulomb gap inside the high electrical field range. However, our experimentally gained values of n are smaller, and the relation $\ln \sigma(E) \propto E^{-1/3}$ is valid. In (28), we did not take into account the field dependence of the pre-exponential part. But consideration of the latter relation will not lead to a substantial approximation between our values of n and the ones given in [8].

As already mentioned in the introduction, the current density versus electrical field relation $j(E)$ is usually analyzed in the high electrical field regime. The investigation of (3) by means of looking at the dependence $w_j(E) = \mathrm{d} \ln j(E)/\mathrm{d}E$ shows that, for the case of the samples 6 and 7, (3) holds with the characteristic value $1/m$ (according to 0.18 and 0.12, respectively). Note that the above values of $1/m$ are substantially smaller than the value 0.5 taken in [15 - 17]. Despite of the fact that the ohmic hopping conductivity (or resistivity, respectively) in the Coulomb gap is described by $\ln \rho(T) \propto T^{-1/2}$, the activationless conductivity in the high electrical field regime obeys the law $\ln \sigma(E) \propto E^{-1/3}$. Thereby, the current density changes like $\ln j(E) \propto E^{-1/6}$. It means that a strong electrical field (in the activationless hopping conductivity regime) is not equivalent to a high temperature (in the ohmic hopping conductivity regime) such that it gives rise to a smaller extent to the increase in conductivity. A similar result was achieved in the experimental work of Aleshin and Shlimak [18].

5. Summary and Conclusions

We have described an experimental preparation technique that is capable to produce mesoscopic carbon network structures with different shapes of the basic cell. There, a drop of the initial polymer solution spreads onto a cooled water surface, and the water vapor interacts with the resulting polymer thin film. Following the self-organization process of precipitating droplets of the water vapor on the polymer layer and subsequently evaporating the solvent, the originally homogeneous polymer film proceeds to a hexagonal network pattern. By the help of an elementary model study on the self-organized structuring process in the liquid polymer films, we succeeded in specifying and interpreting the morphology of the basic network cells observed experimentally.

The dependence of the specific electrical conductivity of self-organized carbon nets on temperature was investigated. Four different transport mechanisms were observed in the temperature range from 4.2 to 295 K. The temperature dependence of the specific resistivity of the carbon network structures, whose conductivity is situated far away from the metal-insulator transition, can be described by $\rho(T) \propto T^{-b} \exp\left([T_0/T]^{(1/p)} \right)$. In the low-temperature range, a Coulomb gap in the density of localized states near the Fermi level occurs with the characteristic value $p = 2$. In the high-temperature range, the pre-exponential part $\rho(T) \propto T^{-b}$ dominates. At intermediate temperatures, Mott's hopping law is observed with $p = 3$. For the samples, the specific resistivity of which is situated near the metal-insulator transition, their behavior in the low-temperature range obeys the power law $\rho(T) \propto T^{-b}$. The value of b decreases from 3 to 0 when looking at samples with a conductivity far away from and near to the metal-insulator transition, respectively. In the high-temperature range, the specific resistivity of the carbon nets is characterized by

$\rho(T) \propto \exp\left(-\left[T/T_1\right]^{c-1}\right)$, with c varying from 1.3 to 1.5. The existence of four charge transport mechanisms can be attributed to tails in the density of localized states, pulled out of the conduction and valence band, as a result of disorder and some overlap between these tails.

In the regime of low temperatures, the charge carrier transport of the porous carbon networks investigated derives from hopping conductivity in the Coulomb gap, described by $\ln \rho(T) \propto T^{-1/2}$. Investigation of the current density versus electrical field characteristic of samples near the metal-insulator transition on the insulating side unveils four distinct regions of field dependence of the conductivity, $\sigma(E)$. At low electrical fields, ohmic conductivity is observed, which does not depend on E. With increasing electrical field, the conductivity rises, first following the law $\ln \sigma(E) \propto E^n$, where n changes from 1.4 to 2.6 with increasing distance from the metal-insulator transition on the insulating side. Upon further raising the electrical field, the conductivity obeys the relation $\ln \sigma(E) \propto E^{1.0}$. The temperature dependence of the

hopping length in that field range can be written as $l(T) \propto T^{-0.9}$. We have demonstrated that at temperatures, where the ohmic conductivity in the Coulomb gap expressed by $\ln \rho(T) \propto T^{-1/2}$ is valid, activationless conductivity at high electrical fields follows the law $\ln \sigma(E) \propto E^{-1/3}$. Accordingly, the current density changes via $\ln j(E) \propto E^{-1/6}$. The disproportion between our experimental data and theory [11] shows that a strong electrical field in the regime of activationless hopping conductivity is not equivalent to a high ambient temperature in the regime of ohmic hopping conductivity. The temperature dependence of the threshold electrical field that characterizes the transition from the low to the high field regime can be extracted by $E_{\text{th}} \propto T^{1.5}$.

Acknowledgements

[1] N. F. Mott and E. A. Davis, Electron Processes in Non-Crystalline Materials, Oxford University Press, Clarendon 1979.

[2] N. F. Mott, J. Non-Cryst. Solids **1**, 1 (1968).

[3] A. L. Efros and B. I. Shklovskii, J. Phys. C: Solid State Phys. **8**, L49 (1975).

[4] A. L. Efros, J. Phys. C: Solid State Phys. **9**, 2021 (1976).

[5] B. I. Shklovskii and A. L. Efros, Electronic Properties of Doped Semiconductors, Springer, Berlin 1984.

[6] R. M. Hill, Phil. Mag. **24**, 1307 (1971).

[7] M. Pollak and I. Riess, J. Phys. C: Solid State Phys. **9**, 2339 (1976).

[8] N. Apsley and H. P. Hughes, Phil. Mag. **31**, 1327 (1975).

[9] N. F. Mott, Phil. Mag. **22**, 7 (1970).

[10] B. I. Shklovskii, Fiz. Tekh. Poluprovodn. **10**, 1440 (1976).

[11] B. I. Shklovskii, Fiz. Tekh. Poluprovodn. **6**, 2335 (1972).

[12] O. Faran and Z. Ovadyahu, Solid State Commun. **67**, 823 (1988).

[13] D. Shahar and Z. Ovadyahu, Phys. Rev. Lett. **64**, 2293 (1990).

[14] R. Rentzsch, I. S. Shlimak, and H. Berger, Phys. Stat. Sol. (a) **54**, 487 (1979).

[15] E. I. Zavaritskaja, Pis'ma Zh. Eksp. Teor. Fiz. **41**, 231 (1985).

[16] F. Tremblay, M. Pepper, R. Newbury, D. Ritchie, D. C. Peacock, J. E. F. Frost, and G. A. C. Jones, Phys. Rev. B **40**, 3387 (1989).

[17] P. Granholm, J. Paloheimo, and H. Stubb, Phys. Stat. Sol. (b) **205**, 315 (1998).

[18] A. N. Aleshin and I. S. Shlimak, Fiz. Tekh. Poluprovodn. **21**, 466 (1987).

[19] T. Bitzer, Honeycomb Technology, Chapman & Hall, London 1997.

[20] S. A. Jenekhe and X. L. Chen, Science **283**, 372 (1999).

[21] Y. Xia, B. Gates, Y. Yin, and Y. Lu, Adv. Mater. **12**, 693 (2000).

[22] D. J. Norris and Yu. A. Vlasov, Adv. Mater. **13**, 371 (2000).

[23] A. Steyer, P. Guenoun, and D. Beysens, Phys. Rev. E. **48**, 428 (1993).

[24] G. Widawski, M. Rawiso, and B. Francois, Nature **369**, 387 (1994).

[25] B. Francois, O. Pitois, and J. Francois, Adv. Mater. **7**, 1041 (1995).

[26] O. Pitois and B. Francois, Eur. Phys. J. B **8**, 225 (1999).

[27] O. Karthaus, N. Maruyama, X. Cieren, M. Shimomura, H. Hasegawa, and T. Hashimoto, Langmuir **16**, 6071 (2000).

[28] M. Srinivasarao, D. Collings, A. Philips, and S. Patel, Science **292**, 79 (2001).

[29] L. V. Govor, I. B. Butylina, I. A. Bashmakov, I. M. Grigorieva, V. K. Ksenevich, and V. A. Samuilov, in: Advanced Semiconductor Devices and Microsystems, edited by T. Labinsky, Smolenice, Slovakia, 1996, p. 81.

[30] L. V. Govor, I. A. Bashmakov, F. N. Kaputski, M. Pientka, and J. Parisi, Macrom. Chem. Phys. **201**, 2721 (2000).

[31] L. V. Govor, I. A. Bashmakov, R. Kiebooms, V. Dyakonov, and J. Parisi, Adv. Mater. **13**, 588 (2001).

[32] A. W. Adamson, Physical Chemistry of Surfaces, John Wiley, New York 1982.

[33] D. Y. C. Chan, J. D. Henry, and L. R. White, J. Colloid Interface Sci. **79**, 410 (1981).

[34] C. M. Knobler and D. Beysens, Europhys. Lett. **6**, 707 (1988).

[35] H. M. Princen, in: Surface and Colloid Science, Vol. 2, edited by E. Matijevic, John Wiley, New York, 1969, p. 1.

[36] D. Beysens and C. M. Knobler, Phys. Rev. Lett. **57**, 1433 (1986).

[37] F. Family and P. Meakin, Phys. Rev. Lett. **61**, 428 (1988).

[38] B. J. Briscoe and K. P. Galvin, J. Phys. D: Appl. Phys. **23**, 422 (1990).

[39] A. V. Limaye, R. D. Narhe, A. M. Dhote, and S. B. Ogale, Phys. Rev. Lett. **79**, 3762 (1996).

[40] A. Steyer, P. Guenoun, and D. Beysens, Phys. Rev. B. **42**, 1086 (1990).

[41] A. G. Zabrodskii, Sov. Phys. Semicond. **11**, 345 (1977).

[42] R. M. Hill, Phys. Stat. Sol. (a) **35**, k29 (1976).

[43] L. V. Govor, M. Goldbach, I. A. Bashmakov, I. B. Butylina, and J. Parisi, Phys. Rev. B **62**, 2201 (2000).

[44] L. V. Govor, I. A. Bashmakov, K. Boehme, M. Pientka, and J. Parisi, J. Appl. Phys. **90**, 1307 (2001).

[45] C. J. Adkins, J. Phys.: Condensed Matter **1**, 1253 (1989).

[46] A. L. Efros and B. I. Shklovskii, Phys. Stat. Sol. (b) **76**, 475 (1976).

[47] T. G. Castner, N. K. Lee, G. S. Cieloszyk, and G. L. Sallinger, Phys. Rev. Lett. **34**, 1627 (1975).

[48] J. H. Davies, P. A. Lee, and T. M. Rice, Phys. Rev. B **29**, 4260 (1984).

[49] H. Vinzelberg, A. Heinrich, C. Gladun, and D. Elefant, Phil. Mag. **65**, 651 (1992).

[50] Y. Zhang, P. Dai, M. Levy, and M. P. Sarachik, Phys. Rev. Lett. **64**, 2687 (1990).

[51] A. W. P. Fung, Z. H. Wang, and M. S. Dresselhaus, Phys. Rev. B **49**, 17325 (1994).

[52] M. H. Cohen, H. Fritzsche, and S. R. Ovshinsky, Phys. Rev. Lett. **22**, 1065 (1969).

[53] L. V. Govor, I. A. Bashmakov, K. Boehme, and J. Parisi, J. Appl. Phys. **91**, 739 (2002).

[54] T. W. Kenny, P. L. Richards, I. S. Park, E. E. Haller, and J. W. Beeman, Phys. Rev. B **39**, 8476 (1989).

[55] E. I. Levin, V. L. Nguyen, and B. I. Shklovskii, Fiz. Tekh. Poluprovodn. **16**, 815 (1982).

[56] E. I. Levin and B. I. Shklovskii, Fiz. Tekh. Poluprovodn. **18**, 856 (1984).